Tomographic reconstruction in soft x-ray microscopy using focus-stack back-projection

Mårten Selin,[1,*] Emelie Fogelqvist,[1] Stephan Werner,[2] and Hans M. Hertz[1]

[1]*Biomedical and X-Ray Physics, Department of Applied Physics, KTH Royal Institute of Technology/Albanova, 10691 Stockholm, Sweden*

[2]*Helmholtz-Zentrum Berlin für Materialien und Energie GmbH, Institute for Soft Matter and Functional Materials, Albert-Einstein-Straße 15, 12489 Berlin, Germany*

**Corresponding author: marten.selin@biox.kth.se*

Received March 9, 2015; revised April 9, 2015; accepted April 15, 2015;
posted April 16, 2015 (Doc. ID 235733); published May 5, 2015

Tomographic reconstruction in soft x-ray microscopy is a powerful technique for obtaining high-resolution 3D images of biological samples. However, the depth of focus of such zone-plate-based microscopes is typically shorter than the thickness of many relevant biological objects, challenging the validity of the projection assumption used in conventional reconstruction algorithms. In order to make full use of the soft x-ray microscopes' high resolution, the tomographic reconstruction needs to take the depth of focus into account. Here we present a method to achieve high resolution in the full sample when the depth of focus is short compared to the sample thickness. The method relies on the back-projection of focus-stacked image data from x-ray microscopy. We demonstrate the method on theoretical and experimental data.

OCIS codes: (100.6950) Tomographic image processing; (340.7460) X-ray microscopy; (110.4980) Partial coherence in imaging.

http://dx.doi.org/10.1364/OL.40.002201

Tomography in water-window x-ray microscopes (XRMs) allows for 3-dimensional (3D) imaging of intact cells in their near-native "hydrated" state with nanoscale resolution [1–5]. The tomographic reconstruction algorithm typically assumes classical projections, i.e., straight line integrals [2–4]. However, in cellular bio-imaging, the XRM depth of focus (DOF) is often shorter than the sample thickness, challenging the validity of the projection assumption. Here we demonstrate a method that improves the reconstruction when the DOF is short compared with the sample thickness, resulting in a higher resolution in the full sample.

Soft x-ray microscopes operating in the water window exploit the natural contrast between carbon and oxygen in the $E = 284$–543 eV energy region ($\lambda = 4.37$–2.29 nm) and rely either on synchrotron sources [3,6,7] or laboratory sources [8]. The imaging is performed with zone plates having a numerical aperture (NA_{zp}) of $\lambda/2\Delta r_N$, where λ is the wavelength, and Δr_N is the outermost zone width [9]. The Rayleigh resolution is $0.61\lambda/NA_{zp}$, and since the DOF is λ/NA_{zp}^2, there is a tradeoff between high resolving power and long DOF. The degree of coherence of the imaging is characterized by the coherence parameter $m = NA_{ill}/NA_{zp}$, where NA_{ill} is the numerical aperture of the condenser illumination. For $m = 0$, the imaging is fully coherent, for $0 < m < 1$ the imaging is partially coherent, and for $m \geq 1$ the imaging can be considered incoherent.

In a typical XRM tomography system, a tilt series of 2D images I_θ are recorded at tilt angles θ. Assuming I_θ are projection data, the 3D volume R can be reconstructed using, e.g., filtered back-projection (FBP) [10]. Here a ramp- or related filter is applied to each image, producing the filtered dataset $\hat{I}_\theta$, which is back-projected over the reconstruction volume as

$$R(x, y, z) = \sum_\theta \hat{I}_\theta(\xi, \eta), \tag{1}$$

where $(\xi, \eta) = M(z \sin\theta + x \cos\theta, y)$ defines the mapping from the image coordinates (ξ, η) at tilt angle θ to the coordinates (x, y, z) in the reconstructed volume at magnification M. Although simple, this method has been very successful in producing results of high biological relevance [1,2]. Iterative methods such as ART, SIRT, etc. are also widely used [4,11], notably due to their better capabilities to incorporate regularization conditions and cope with missing data. However, all methods discussed above assume projection data, constraining the experimental parameters to cases where the projection assumption is sufficiently valid. Figure 1 illustrates a situation where the DOF is shorter than the object thickness, weakening the validity of the projection assumption since the whole volume cannot be simultaneously imaged sharply. Many bio-samples studied with XRM

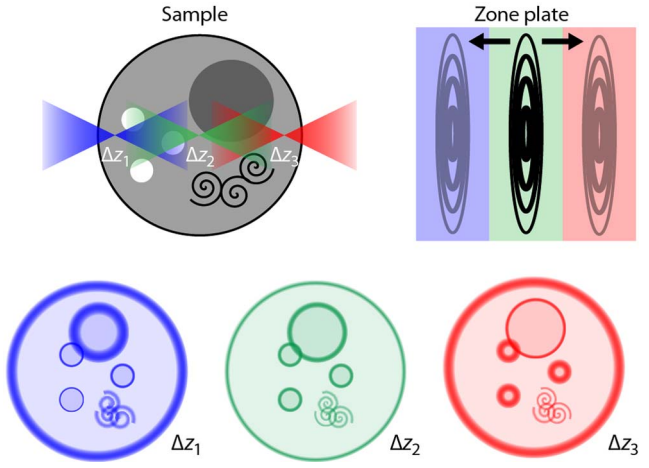

Fig. 1. Illustrating the problem of a depth of focus (DOF) smaller than the sample thickness. With high NA-optics, not all features are simultaneously in focus. The sample–zone plate distance determines the amount of defocus Δz in the sample volume.

tomography are thicker than the DOF of high-resolution zone plates [3,5], and some experiments have therefore settled for a lower-resolution zone plate in order to better fulfill the DOF requirement [4].

There have been attempts to develop improved reconstruction methods for XRM tomography [12,13], but experimental success has yet to be demonstrated, and the validity of the used forward model is under discussion [14]. The DOF problem is also present in optical microscopy, where techniques such as wavelet-based image fusion [15] and deconvolution microscopy [16] are employed to obtain an overall sharper image and a 3D image, respectively. However, these methods have not been explored for tomography.

In tomographic electron microscopy of thin objects, there are methods to correct for object planes extending outside the DOF when tilting [17]. For thick objects, "Defocus-gradient corrected back-projection" (DGCBP) [18] may greatly improve the quality of the reconstructed data.

In DGCBP the images I_θ in the tomographic data set are deconvolved with a defocus-dependent PSF $h_{\Delta z}$ before they are filtered and back-projected as in FBP according to

$$R(x,y,z) = \sum_\theta \overline{I_\theta(\xi,\eta) \otimes^{-1} h_{\Delta z}(\xi,\eta)}, \tag{2}$$

where $\Delta z = z\cos\theta + x\sin\theta$ defines the defocus position in the reconstruction volume, and $\otimes^{-1}$ denotes deconvolution.

In the present paper, we demonstrate FSBP—focus-stack back-projection. Figure 2 illustrates the method. This novel reconstruction method for XRM tomography makes use of an experimentally acquired focus stack $I_{\theta,1}, I_{\theta,2} \ldots I_{\theta,S}$ at S defocus positions $\Delta z_1, \Delta z_2, \ldots \Delta z_S$ for each tilt angle. As in the previously discussed

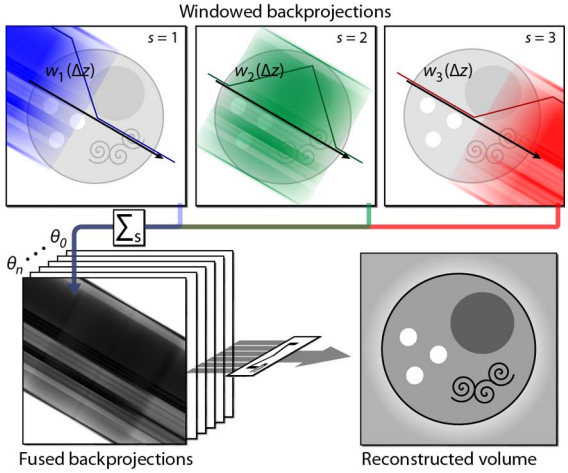

Fig. 2. Focus-stack back-projection (FSBP) with the focus stacks at 3 defocus positions for each tilt angle in the tomographic data set. Each image in the focus stack is filtered, back-projected, and weighted with a longitudinal window function, forming a windowed back-projection. The windowed back-projections are fused for every tilt angle, before proceeding with a sum over all angles as in the filtered back-projection algorithm (FBP).

methods the images are first appropriately filtered, producing the filtered dataset $\hat{I}_{\theta,s}$, for all tilt angles and defocus positions. By forming a linear combination of all back-projections of the images in the filtered dataset, where each back-projection is subject to a weighting function w_s operating in the defocus direction, the reconstruction is performed as

$$R(x,y,z) = \sum_\theta \sum_s \hat{I}_{\theta,s}(\xi,\eta) \times w_s(\Delta z). \tag{3}$$

The voxel dependent weighting factors $w_s(\Delta z)$ are chosen so that the total weight assigned to each voxel in the reconstruction volume equals 1. One natural choice of weighting factors is a set of asymmetric triangle functions:

$$w_s(\Delta z) = \begin{cases} (\Delta z - \Delta z_{s-1})/(\Delta z_s - \Delta z_{s-1}), & \Delta z_{s-1} < \Delta z \le \Delta z_s \\ (\Delta z - \Delta z_{s+1})/(\Delta z_s - \Delta z_{s+1}), & \Delta z_s < \Delta z \le \Delta z_{s+1}, \\ 0, & \text{else} \end{cases} \tag{4}$$

with $\Delta z_0 = -\infty$ and $\Delta z_{S+1} = +\infty$.

We will not give a rigorous proof of the proper operation of the FSBP method, but a qualitative argument can be made as follows: With sufficient sampling in the defocus direction, every feature will be sharply imaged in at least one image in the focus stack for every tilt angle. During reconstruction, those images will all act on the sub-volume where the feature is located, thus achieving a sharp local reconstruction. Although this does not provide formal criteria defining the range of validity of the method, the simulations and experiments presented below indicate that the method works well for the typical high-resolution imaging task.

In Fig. 3, we compare the effectiveness of the FBP, DGCBP, and FSBP reconstruction methods at different microscope parameters. The comparison is performed for the water-and-carbon phantom of Fig. 3, where the carbon content is 10% for the shell and 50% for the 50–200 nm spheres. For a 20-nm zone plate ($NA_{zp} = 0.06$), simulations were made with condenser illumination $NA_{ill} = 0.02$ (Figs. 3(a), 3(c), and 3(e)) and $NA_{ill} = 0.06$ (Figs. 3(b), 3(d), and 3(f)). For a 40-nm zone plate ($NA_{zp} = 0.03$), simulations were made with condenser illumination $NA_{ill} = 0.02$ (Figs. 3(g)–3(i)), corresponding to the experimental parameters of Fig. 4.

Simulations start with generating a tomographic data set using the 3D wave propagation method of Ref. [14]. This data set is at $\lambda = 2.4$ nm, in 1° steps over 0°–179°, with the focus stack at three defocus positions −3, 0, +3 μm. To include the effect of photon noise, Poisson distributed noise is added to each simulated image. For a fair comparison, the FSBP method divides its photons among the images in one focus stack, i.e., all methods use the same total dose. All three methods are compared at two condenser settings and two levels of photon flux incident on the sample, 7×10^7 ph/μm^2/proj. and 7×10^9ph/μm^2/proj., and assuming a zone plate efficiency of 5%.

We first compare the algorithms for the 20-nm zone-plate case, Figs. 3(a)–3(f). In the classical FBP

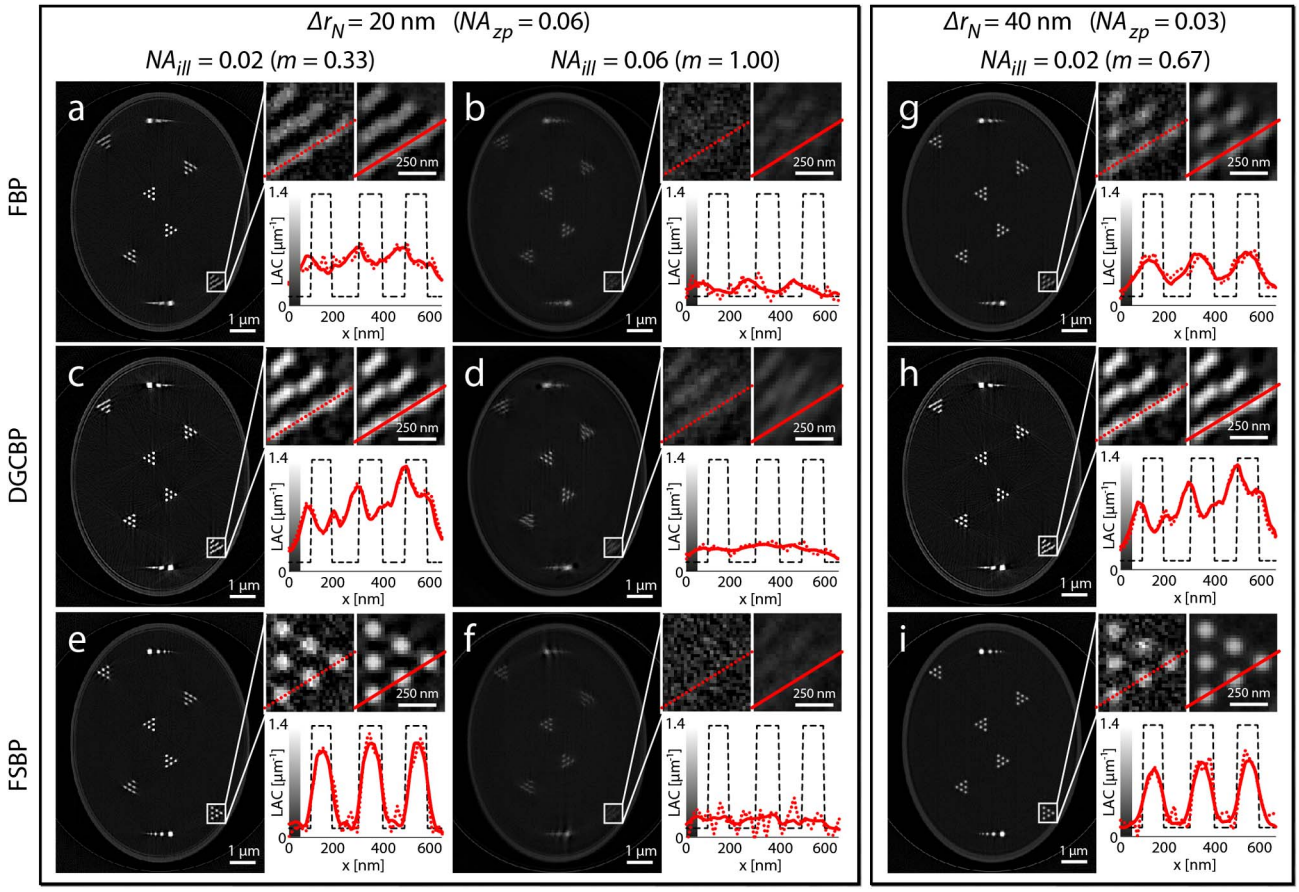

Fig. 3. Comparison of reconstruction methods on simulated tomographic data sets with different microscope parameters at $\lambda = 2.4$ nm. The zone plate has outermost zone width 20 nm in (a)–(f) and 40 nm in (g)–(i). The condenser illumination has NA = 0.02 in (a), (c), (e) and (g)–(i) and 0.06 in (b), (d) and (f). The different combination of microscope parameters of each column yields the values 0.33, 1.00, and 0.67, respectively, for the coherence parameter $m = NA_{ill}/NA_{zp}$. The reconstructions in (a), (b), and (g) are performed with FBP, (c), (d), and (h) are performed with DGCBP and (e), (f), and (i) are performed with FSBP. The insets in each sub-figure show a magnified view of the region in the white rectangle at two noise levels. For a fair comparison between the methods, the simulated recordings are made at the same total dose delivered to the sample: 7×10^7 ph/µm^2/proj. angle (dotted line), 7×10^9 ph/µm^2 proj. angle (solid line).

reconstruction, there are artifacts that increase with distance from the rotation center. At distances >3 µm, the tangential resolution is severely lowered by elongation artifacts, and the line profiles exhibit phase shifts at $NA_{ill} = 0.02$ [Fig. 3(a)] and contrast reversal at $NA_{ill} = 0.06$ [Fig. 3(b)].

The DGCBP reconstruction algorithm improves contrast at $NA_{ill} = 0.02$ [Fig. 3(c)], but still suffers from the same artifacts as FBP in the tangential direction. At $NA_{ill} = 0.06$ [Fig. 3(d)] the contrast enhancement is lost.

Our FSBP reconstruction algorithm produces a significant improvement in reconstruction, even at lower signal conditions, albeit only for the $NA_{ill} = 0.02$ – data [Fig. 3(e)]. For the $NA_{ill} = 0.06$ – data [Fig. 3(f)], the contrast is severely degraded, but the method does not exhibit the contrast reversal of FBP at the same parameters.

For low m-values ($NA_{ill}/NA_{zp} = 0.02/0.06$), the FSBP clearly produces superior reconstructions. This is probably due to the somewhat longer DOF and higher contrast that the partial coherence leads to. For higher m-values ($NA_{ill}/NA_{zp} = 0.06/0.06$), the difference between the methods is less. We note that increasing the range and sampling density in the focus stacks did not improve FSBP's reconstructions noticeably for the case. These observations support claims that partially coherent illumination may be desirable for high-resolution XRM tomography [2,3] despite the fact that the $m = 1$ case is often cited as the preferred [6,7].

As expected, FBP produces a better reconstruction for the 40 nm zone-plate data [Fig. 3(g)] due to the longer DOF, albeit at low contrast. The artifacts in DGCBP were not mitigated, however [Fig. 3(h)]. FSBP again greatly improves the quality of the reconstruction [Fig. 3(i)], but not as much as in the more coherent $NA_{ill}/NA_{zp} = 0.02/0.06$ case.

To confirm our theoretical findings, we collected a full tomographic data set including a focus stack at each tilt angle at the HZB Transmission X-ray Microscope in Berlin [3]. The object is a pair of overlapping diatom frustules occupying an area of ~13 µm × 8 µm perpendicular to the rotation axis. The silica-rich frustules contain both larger structures, such as valves and ribs, and smaller structures, such as pores. The spatial scales are typical for wet bio-samples, while the contrast is larger than bio-samples normally exhibit.

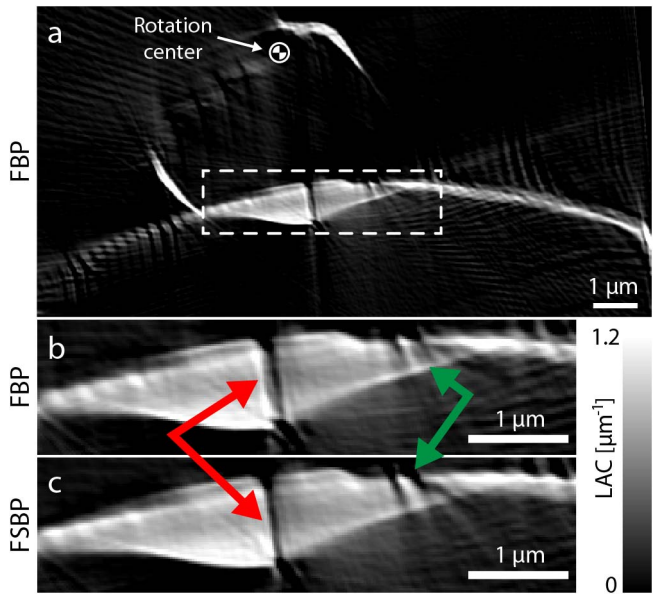

Fig. 4. One slice from the reconstruction of the diatom frustules (a). Insets (b) and (c) show magnified views of a frustule rib at 3–5 μm from the rotation axis from data reconstructed with FBP and FSBP, respectively. Tangential blur in the FBP data is removed in the FSBP-data, here visible at the raphe (red arrows) and pore structures (green arrows).

The frustule-pair was imaged at 510 eV ($\lambda = 2.4$ nm) with a 40-nm zone plate. The resulting numerical aperture of the zone plate is $NA_{zp} = 0.03$, and the DOF is 2.7 μm. The numerical aperture of the condenser is $NA_{ill} = 0.02$, yielding the coherence parameter $m = NA_{ill}/NA_{zp} = 0.67$. The zone plate and condenser parameters thus match the theoretical used in Figs. 3(g)–3(i). Images were acquired at tilt-angles $-55° - +55°$ in 1° steps with 1-second exposures. All images were background corrected with a measured flatfield intensity image, and aligned to the rotation axis. Reconstructions were performed using FBP with the $\Delta z = 0$ μm image, and using FSBP with the $\Delta z = -3$ μm, 0 μm, +3 μm images at each tilt angle, and with $\Delta z = 0$ μm defined as the plane containing the tilt axis. A slice of the reconstructed volume perpendicular to the rotation axis is shown in Fig. 4(a), and Figs. 4(b)–4(c) shows a magnified view of a frustule rib at distance 3–5 μm from the rotation center reconstructed with FBP and FSBP, respectively.

The tangential blur of FBP that is observed in the simulations [Fig. 3(a)] is also present in the experiments [cf. arrows in Fig. 4(b)]. As in the simulations, the artifacts seem to be eliminated with the FSBP algorithm, thereby increasing the resolution in the reconstructed data. However, artifacts are still present because of the missing wedge of 70° in the experimental tomographic data set. Furthermore, image alignment was performed as carefully as possible, but streaks in the reconstructed data indicate that it was not perfect. Still, FSBP offers a significant improvement in reconstruction quality on the features considered.

To conclude, we have demonstrated that our FSBP algorithm utilizing focus stacks improves the resolution and quality in XRM tomographic reconstructions for the partially coherent imaging case. The algorithm is demonstrated on theoretical as well as experimental data. Furthermore, it appears as the increased partial coherence that comes from using higher-resolution zone plates can be a desired property in XRM tomography, when taken properly into account in the reconstruction algorithm. Consequently, FSBP unlocks the higher resolution power available to XRMs for 3D bio-imaging. The method comes at no cost as regards dose but increases the number of images that needs to be acquired. However, our results show that this increase may well be worth the effort considering the gain in resolution over the full volume.

We thank U. Vogt of KTH and P. Guttmann, K. Henzler, S. Rehbein, and G. Schneider of HZB for valuable discussions and/or beamline support. We thank HZB for the allocation of synchrotron radiation beam time. This work was financially supported by the Swedish Research Council Röntgen Ångström program.

References

1. C. A. Larabell and M. A. Le Gros, Mol. Biol. Cell **15**, 957 (2004).
2. J. L. Carrascosa, F. J. Chichon, E. Pereiro, M. J. Rodriguez, J. J. Fernandez, M. Esteban, S. Heim, P. Guttmann, and G. Schneider, J. Struct. Biol. **168**, 234 (2009).
3. G. Schneider, P. Guttmann, S. Heim, S. Rehbein, F. Mueller, K. Nagashima, J. Heymann, W. Müller, and J. McNally, Nat. Methods **7**, 985 (2010).
4. F. J. Chichon, M. J. Rodriguez, E. Pereiro, M. Chiappi, B. Perdiguero, P. Guttmann, S. Werner, S. Rehbein, G. Schneider, M. Esteban, and J. L. Carrascosa, J. Struct. Biol. **177**, 202 (2012).
5. R. Carzaniga, M. C. Domart, L. M. Collinson, and E. Duke, Protoplasma **251**, 449 (2014).
6. M. A. Le Gros, G. McDermott, B. P. Cinquin, E. A. Smith, M. Do, W. Chao, P. P. Naulleau, and C. Larabell, J. Synchrotron Radiat. **21**, 1370 (2014).
7. E. Pereiro, J. Nicolas, S. Ferrer, and M. R. Howells, J. Synchrotron Radiat. **16**, 505 (2009).
8. H. M. Hertz, O. von Hofsten, M. Bertilson, U. Vogt, A. Holmberg, J. Reinspach, D. Martz, M. Selin, A. E. Christakou, J. Jerlstrom-Hultqvist, and S. Svard, J. Struct. Biol. **177**, 267 (2012).
9. D. Attwood, *Soft X-Rays and Extreme Ultraviolet Radiation: Principles and Applications* (Cambridge University, 2007).
10. A. C. Kak and M. Slaney, *Principles of Computerized Tomographic Imaging* (IEEE, 1988).
11. M. Bertilson, O. von Hofsten, U. Vogt, A. Holmberg, A. E. Christakou, and H. M. Hertz, Opt. Lett. **36**, 2728 (2011).
12. J. Oton, C. O. Sorzano, E. Pereiro, J. Cuenca-Alba, R. Navarro, J. M. Carazo, and R. Marabini, J. Struct. Biol. **178**, 29 (2012).
13. J. Klukowska, G. T. Herman, J. Oton, R. Marabini, and J. M. Carazo, Inverse Problems **30**, 125015 (2014).
14. M. Selin, E. Fogelqvist, A. Holmberg, P. Guttmann, U. Vogt, and H. M. Hertz, Opt. Express **22**, 30756 (2014).
15. A. G. Valdecasas, D. Marshall, J. M. Becerra, and J. J. Terrero, Micron **32**, 559 (2001).
16. J. G. McNally, T. Karpova, J. Cooper, and J. A. Conchello, Methods **19**, 373 (1999).
17. H. Winkler and K. A. Taylor, J. Struct. Biol. **143**, 24 (2003).
18. G. J. Jensen and R. D. Kornberg, Ultramicroscopy **84**, 57 (2000).